A photonic-crystal optical antenna for extremely large local-field enhancement

Hyun-Joo Chang,[1,2] Se-Heon Kim,[3,4,*] Yong-Hee Lee,[1] Emil P. Kartalov,[2,4] and Axel Scherer[3,4]

[1]*Department of Physics, Korea Advanced Institute of Science and Technology (KAIST), Daejeon 305-701, Korea.*
[2]*Department of Pathology, Keck School of Medicine, University of Southern California, Los Angeles, CA 90033, USA.*
[3]*Kavli Nanoscience Institute, California Institute of Technology, Pasadena, CA 91125, USA.*
[4]*Electrical Engineering, Mail Code 200-36, California Institute of Technology, Pasadena, CA 91125, USA.*
**seheon@caltech.edu*

Abstract: We propose a novel design of an all-dielectric optical antenna based on photonic-band-gap confinement. Specifically, we have engineered the photonic-crystal dipole mode to have broad spectral response (Q ~70) and well-directed vertical-radiation by introducing a plane mirror below the cavity. Considerably large local electric-field intensity enhancement ~4,500 is expected from the proposed design for a normally incident planewave. Furthermore, an analytic model developed based on coupled-mode theory predicts that the electric-field intensity enhancement can easily be over 100,000 by employing reasonably high-Q (~10,000) resonators.

OCIS codes: (160.5293) Photonic bandgap materials; (190.4360) Nonlinear optics, devices; (230.5298) Photonic crystals; (230.5750) Resonators; (290.5825) Scattering theory.

References and links

1. K. B. Crozier, A. Sundaramurthy, G. S. Kino, and C. F. Quate, "Optical antennas: Resonators for local field enhancement," J. Appl. Phys. **94**, 4632–4642 (2003).
2. P. Mühlschlegel, H.-J. Eisler, O. J. F. Martin, B. Hecht, and D. W. Pohl, "Resonant optical antennas," Science **308**(5728), 1607–1609 (2005).
3. E. Cubukcu, E. A. Kort, K. B. Crozier, and F. Capasso, "Plasmonic laser antenna," Appl. Phys. Lett. **89**, 093120 (2006).
4. C. Sönnichsen, T. Franzl, T. Wilk, G. von Plessen, J. Feldmann, O. Wilson, and P. Mulvaney, "Drastic reduction of plasmon damping in gold nanorods," Phys. Rev. Lett. **88**(7), 077402 (2002).
5. T. Kosako, Y. Kadoya, and H. F. Hofmann, "Directional control of light by a nano-optical Yagi-Uda antenna," Nat. Photonics **4**, 312–315 (2010).
6. Y. Lu, G. L. Liu, J. Kim, Y. X. Mejia, and L. P. Lee, "Nanophotonic crescent moon structures with sharp edge for ultrasensitive biomolecular detection by local electromagnetic field enhancement effect," Nano Lett. **5**(1), 119–124 (2005).
7. K. Kneipp, *et al*., "Single molecule detection using surface-enhanced Raman scattering (SERS)," Phys. Rev. Lett. **78**, 1667–1670 (1997).
8. A. Bouhelier, M. Beversluis, A. Hartschuh, and L. Novotny, "Near-field second-harmonic generation induced by local field enhancement," Phys. Rev. Lett. **90**(1), 013903 (2003).
9. S. Kim, J. Jin, Y. J. Kim, I. Y. Park, Y. Kim, and S. W. Kim, "High-harmonic generation by resonant plasmon field enhancement," Nature **453**(7196), 757–760 (2008).
10. E. Prodan, and P. Nordlander, "Plasmon hybridization in spherical nanoparticles," J. Chem. Phys. **120**(11), 5444–5454 (2004).
11. O. Painter, J. Vuckovic, and A. Scherer, "Defect modes of a two-dimensional photonic crystal in an optically thin dielectric slab," J. Opt. Soc. Am. B **16**, 275–285 (1999).
12. E. Yablonovitch, "Inhibited spontaneous emission in solid-state physics and electronics," Phys. Rev. Lett. **58**(20), 2059–2062 (1987).
13. H.-Y. Ryu, M. Notomi, and Y.-H. Lee, "High-quality-factor and small-mode-volume hexapole modes in photonic-crystal-slab nanocavities," Appl. Phys. Lett. **83**, 4294–4296 (2003).
14. S. Noda, M. Fujita, and T. Asano, "Spontaneous-emission control by photonic crystals and nanocavities," Nature photon. **1**, 449–458 (2007).
15. T. Tanabe, M. Notomi, E. Kuramochi, A. Shinya, and H. Taniyama, "Trapping and delaying photons for one nanosecond in an ultrasmall high-Q photonic-crystal nanocavity," Nat. Photonics **1**, 49–52 (2007).
16. S.-H. Kim, S.-K. Kim, and Y.-H. Lee, "Vertical beaming of wavelength-small photonic crystal resonators," Phys. Rev. B **73**, 235117 (2006).

#135050 - $15.00 USD Received 13 Sep 2010; revised 16 Oct 2010; accepted 21 Oct 2010; published 3 Nov 2010

17. S. Fan, W. Suh, and J. D. Joannopoulos, "Temporal coupled-mode theory for the Fano resonance in optical resonators," J. Opt. Soc. Am. A **20**(3), 569–572 (2003).
18. R. E. Hamam, A. Karalis, J. D. Joannopoulos, and M. Soljacic, "Coupled-mode theory for general free-space resonant scattering of waves," Phys. Rev. A **75**, 053801 (2007).
19. C. A. Balanis, *Antenna Theory: Analyses and Design* (John Wiley and Sons, Inc., Hoboken, New Jersey, 2005).
20. E. M. Purcell, "Spontaneous emission probabilities at radio frequencies," Phys. Rev. **69**, 681 (1946).
21. A. Campion, and P. Kambhampati, "Surface-enhanced Raman scattering," Chem. Soc. Rev. **27**, 241–250 (1998).
22. J. T. Robinson, C. Manolatou, L. Chen, and M. Lipson, "Ultrasmall mode volumes in dielectric optical microcavities," Phys. Rev. Lett. **95**(14), 143901 (2005).
23. M. Loncar, A. Scherer, and Y. Qiu, "Photonic crystal laser sources for chemical detection," Appl. Phys. Lett. **82**, 4648–4650 (2003).
24. A. Taflove, and S. C. Hagness, *Computational Electrodynamics: the Finite-Difference Time-Domain Method* (2nd ed) (Artech House, 2000).
25. J. Aizpurua, P. Hanarp, D. S. Sutherland, M. Käll, G. W. Bryant, and F. J. García de Abajo, "Optical properties of gold nanorings," Phys. Rev. Lett. **90**(5), 057401 (2003).
26. H. Wang, D. W. Brandl, F. Le, P. Nordlander, and N. J. Halas, "Nanorice: a hybrid plasmonic nanostructure," Nano Lett. **6**(4), 827–832 (2006).
27. A. Rodriguez, M. Soljacic, J. D. Joannopoulos, and S. G. Johnson, "$\chi^{(2)}$ and $\chi^{(3)}$ harmonic generation at a critical power in inhomogeneous doubly resonant cavities," Opt. Express **15**(12), 7303–7318 (2007).
28. B. Tian, X. Zheng, T. J. Kempa, Y. Fang, N. Yu, G. Yu, J. Huang, and C. M. Lieber, "Coaxial silicon nanowires as solar cells and nanoelectronic power sources," Nature **449**(7164), 885–889 (2007).
29. S. G. Johnson, *http://ab-initio.mit.edu/wiki/index.php/Harminv*

1. Introduction

In analogy to the radio-frequency antenna, an optical antenna can function either as a transmitter (emitter) or a receiver in the optical frequency domain. For use as a receiver, incident electromagnetic wave's energy shall be efficiently captured by the antenna at a certain resonance condition, resulting in strongly-enhanced local-electromagnetic-fields. Recently, various metallic nano-antennas have been proposed and demonstrated [1–6] to obtain such strong local-fields (or hot-spots) for bio-chemical sensing applications [6,7] and for boosting a wide range of nonlinear optics phenomena [8,9]. However, the performance of these antennas is often limited by their low Q < ~20, which is due to either huge radiation losses or absorption losses in the metallic structure itself [4]. Moreover, it has been known that resonance frequencies of plasmonic nanostructures do not have a strong dependence on scale [10], which makes it challenging to develop an array of diverse plasmonic resonances.

In this paper, we propose to use a 2-D photonic-crystal (PhC) slab structure [11] as a novel platform for the efficient optical antenna with strong local field enhancement. Until now, various 2-D PhC cavities have been extensively researched for achieving ultrasmall mode-volume (V) and high-Q enabled by the photonic-band-gap (PBG) in the in-plane directions [11–15]. Evidently, such non-metallic PhC cavities can provide much higher-Q (easily over 10,000) in comparison with their metallic counterparts. Furthermore, the resonances of PhC cavities are scalable with the lattice constant, allowing lithographic means to tune the resonances and to integrate them in a dense array within a small footprint.

2. Coupled mode theory for photonic-crystal optical antennas

Our scheme for a PhC optical antenna is shown in Fig. 1(a). A high-permittivity semiconductor PhC slab cavity is positioned nearby a plane mirror. By varying the gap distance, d, one can control the directionality of the far-field emission, which in turn will be used to optimize the antenna coupling efficiency [16]. An electromagnetic planewave with intensity I_0 is being illuminated at a normal direction ($\theta = 0$), where the incident electric-field is polarized along the x-axis. To understand the underlying physics, we first consider a simplified model in the spirit of coupled-mode theory (CMT) [17,18] as described in Fig. 1(b). The energy amplitude in the cavity denoted by α is being built up by the incident planewave while decaying into (infinitely many) multiple 'ports', which are imaginary two-way waveguides connecting the near-zone to the far-zone and vice versa. A symbol 'k' is assigned to the port lying in the direction of $k = (\theta, \phi)$. The port k is extended within a differential solid angle, $d\Omega(\theta, \phi)$, at around $k = (\theta, \phi)$. We have especially assigned a

#135050 - $15.00 USD Received 13 Sep 2010; revised 16 Oct 2010; accepted 21 Oct 2010; published 3 Nov 2010

symbol '0' to the port at a normal direction ($\theta = 0$). The CMT master equation describing how α is evolved in time is given by [17]

$$\frac{d\alpha}{dt} = i\omega_c \alpha - \left(\frac{1}{\tau_{tot}}\right)\alpha + \kappa_0 S_{+0} \ . \tag{1}$$

Here ω_c and $1/\tau_{tot}$ (i.e., $Q_{tot} = \omega_c \tau_{tot}/2$) are the resonant frequency and the total decay rate of α, respectively. The total electromagnetic energy in the cavity is given by $|\alpha|^2$. The coupling from the planewave is described by the last two terms, κ_0 and S_{+0}. For the planewave with an area of A, incident energy per unit time (power) to the 'port 0' is $\left\langle |S_{+0}|^2 \right\rangle_T = I_0 A = (1/2) c\varepsilon_0 n_{bg} |\vec{E}_0|^2 A$, where ε_0 and n_{bg} are the permittivity of vacuum and the refractive index of the background medium, respectively and $\langle \ \rangle_T$ denotes a time average over one optical cycle. Only a small fraction of the power, $|S_{+0}|^2$, will be coupled to the

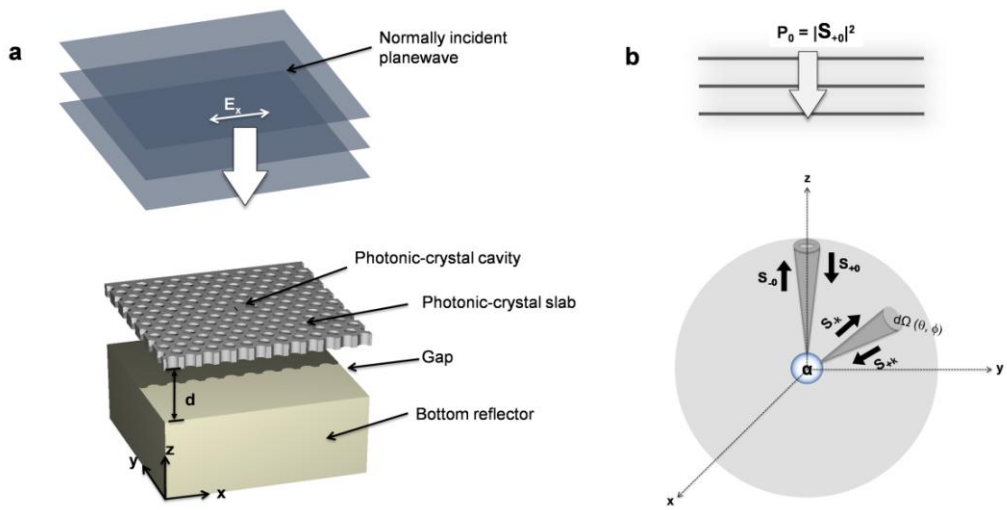

Fig. 1. All-dielectric photonic-crystal (PhC) antenna. (a) The 2-D PhC cavity is placed at a distance of *d* from the reflector. The linearly-polarized planewave is being illuminated from the top. (b) A coupled-mode theory diagram describes interaction between the incident planewave and the PhC cavity. The port *k* is defined for an imaginary two-way waveguide in the direction of $k = (\theta, \phi)$ with an angular extent defined by a differential solid angle, $d\Omega(\theta, \phi)$. α represents the energy amplitude of the cavity. S_{+k} and S_{-k} are the power amplitudes propagating in the port *k*. The PhC antenna is excited only through the 'port 0' with carried power of $|S_{+0}|^2$.

resonant mode, which is described by using the coupling constant, κ_0. According to the CMT, κ_0 can be expressed in terms of $1/\tau_0$, the partial decay rate of α only through the port 0. Note that although κ_0 is an infinitesimally small value, S_{+0} and A are infinitely large for an ideal planewave. Hence their product form of $|\kappa_0|^2 A$ becomes a certain finite value (see Appendix A).

Under continuous excitation, $|\alpha|^2$ rapidly grows within the time proportional to $\sim Q_{tot}/\omega_c$, then reaches a certain steady-state value. This saturation energy is obtained from Eq. (1),

#135050 - $15.00 USD Received 13 Sep 2010; revised 16 Oct 2010; accepted 21 Oct 2010; published 3 Nov 2010

$$\left\langle |\alpha|^2 \right\rangle_T \Big|_{t\to\infty} = \tau_{tot}^2 \left|\kappa_0\right|^2 \left\langle \left|S_{+0}\right|^2 \right\rangle_T = \frac{1}{2} c\varepsilon_0 n_{bg} \tau_{tot}^2 \left|\vec{E}_0\right|^2 \cdot \left|\kappa_0\right|^2 A \ . \tag{2}$$

Note that the above equation contains the electric-field intensity of the incident wave, $\left|\vec{E}_0\right|^2$. Another equivalent expression to the above equation can be obtained from the cavity quantum electrodynamics (cQED) definition of the mode volume (see Appendix B),

$$\left\langle \left|\alpha\right|^2 \right\rangle_T \Big|_{t\to\infty} = \frac{1}{2} V_m \varepsilon_0 n_c^2 \left|\vec{E}_{loc}\right|^2 , \tag{3}$$

which now includes the maximum electric-field intensity in the cavity. To facilitate an explicit expression for $\left|\kappa_0\right|^2 A$, we introduce a new term, namely 'far-field coupling factor' [19],

$$\eta(\theta,\phi) \equiv \frac{\dfrac{dP}{d\Omega}(\theta,\phi)}{P_{tot}}, \tag{4}$$

which is the ratio between the power radiated per unit solid angle in the direction of $k = (\theta,\phi)$ and the total radiated power, P_{tot}. One can easily show that this dimensionless quantity varies from 0 to 1 and has the property such that $\int \eta(\theta,\phi) d\Omega = 1$. Furthermore, it can also be shown that, for a normally incident planewave, the product term, $\left|\kappa_0\right|^2 A$, is directly proportional to $\eta(\theta = 0)$ (see Appendix A) such that

$$\left|\kappa_0\right|^2 A = \frac{2}{\tau_{tot}} \cdot \left(\frac{\lambda}{n_{bg}}\right)^2 \cdot \eta(\theta = 0) \cdot \cos^2 \chi \ . \tag{5}$$

Combining Eqs. (2), (3), and (5), finally, we obtain the electric-field intensity enhancement factor,

$$\Phi_I \equiv \frac{\left|\vec{E}_{loc}\right|^2}{\left|\vec{E}_0\right|^2} = \frac{2}{\pi} \cdot \frac{\lambda^3}{n_{bg} \cdot n_c^2} \cdot \frac{Q_{tot}}{V_m} \cdot \eta(\theta = 0) \cdot \cos^2 \chi \ . \tag{6}$$

This result shows that Φ_I is proportional to both Q_{tot}/V_m and η. Therefore, a PhC cavity with the larger Purcell factor [20] is more advantageous for the higher Φ_I. However, for a resonant mode that has null vertical emission, $\eta(\theta = 0) = 0$, or an incident planewave with $\chi = \pi / 2$, there is no enhancement ($\Phi_I = 0$) regardless of how large Purcell factor is used. It may be noted that Q_{tot} and $\eta(\theta = 0)$ are not independent each other because $\eta(\theta = 0)$ is an implicit function of Q_{tot} (since $Q_{tot} = \omega\left|\alpha\right|^2 / P_{tot}$). We also note that most high-Q PhC cavities (Q_{tot} > 100,000) have either null vertical emission or very poor directionality [13]. Therefore, we expect a certain trade-off relationship between Q_{tot} and $\eta(\theta = 0)$. In practical applications, the maximum Q_{tot} may be limited by the bandwidth ($\Delta\omega$) requirement. For example, for nonlinear optics applications, where efficient light generation at frequencies

#135050 - $15.00 USD Received 13 Sep 2010; revised 16 Oct 2010; accepted 21 Oct 2010; published 3 Nov 2010

different from that of a pumping beam is required, the bandwidth may be chosen to cover the wide enough frequency range of interests [6–9].

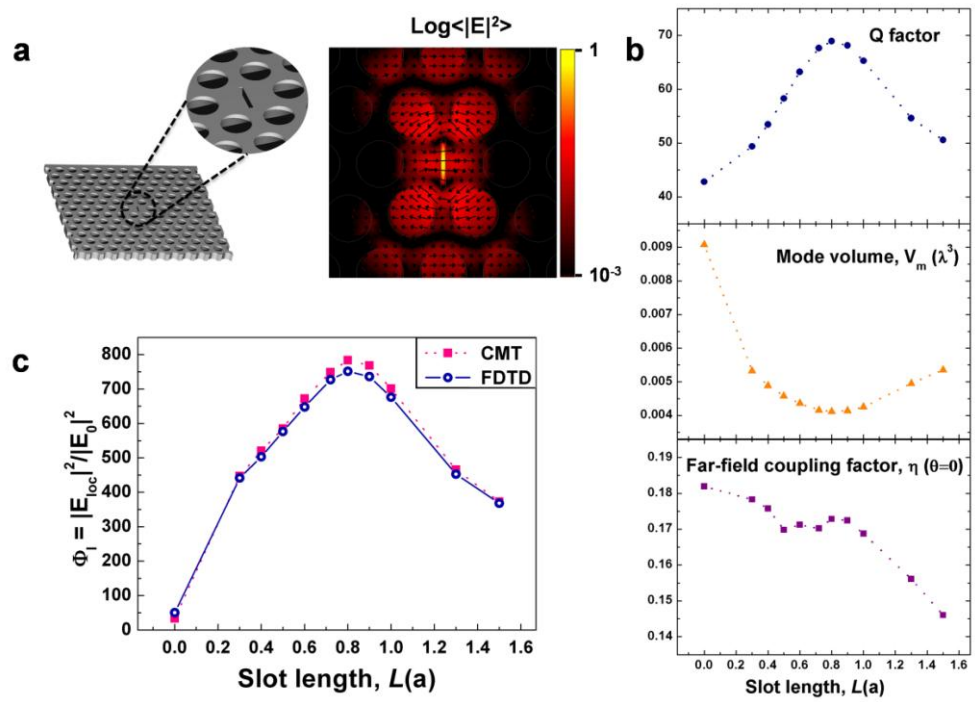

Fig. 2. Effects of the nano-slot on local-field enhancement. The photonic-crystal (PhC) cavity is completely immersed in water (n_{bg} = 1.33), where the bottom reflector is excluded. (a) The left panel shows a schematic illustration of the nano-slot positioned at the center of the PhC cavity. The nano-slot has a rectangular geometry whose width is fixed to 0.05 a while its length, *L*, is to be varied. The right panel shows electric-field intensity ($|\vec{E}|^2$) distribution around the nano-slot. (b) Quality factor, Q_{tot}, mode volume, V_m, and the far-field coupling factor, $\eta(\theta = 0)$, calculated as a function of *L*. (c) The electric-field intensity enhancement factors, Φ_l , obtained from the coupled-mode theory (CMT) are compared with those obtained from the rigorous finite-difference time-domain (FDTD) simulation. The maximum Φ_l of ~750 (~783) is obtained from CMT (FDTD) at *L* = 0.8 a.

3. Design of a photonic-crystal optical antenna

3.1 Effects of a nano-slot

As a practical example, we have designed a compact, stand-alone, label-free Raman sensor [7,21] operating at a wavelength of ~1 μm. For this purpose, however, Q_{tot} should usually be limited by ~100 in consideration of typical magnitudes of Stokes energy shifts. Designing such a low-*Q* PhC cavity could be challenging as it should have both moderately large $\eta(\theta = 0)$ and small V_m .

Figure 2(a) shows our design, where the conventional single-defect PhC cavity (also known as H1) has been modified (see Appendix C). The nano-slot structure introduced in the centre of the cavity creates highly-concentrated electromagnetic-fields inside the gap so that it can be used to optimize the overlap with an analyte molecule [22,23]. Hereafter, the entire PhC cavity is assumed to be immersed in a medium having a refractive index of 1.33 (that of

#135050 - $15.00 USD Received 13 Sep 2010; revised 16 Oct 2010; accepted 21 Oct 2010; published 3 Nov 2010

water) for real-time sensing applications. The three key parameters, Q_{tot}, V_m, and η, (see Fig. 2(b)) can be obtained by using the finite-difference time-domain method (FDTD) [24]. Note that far-field emission from our PhC cavity mode is *x*-polarized at $\theta = 0$ hence $\chi = 0$ in Eq. (6).

First, we consider a PhC cavity without having a bottom reflector. The length of the nano-slot, *L*, is varied while the width of it has been fixed to 0.05 a, which corresponds to ~20 nm for the operational wavelength (see Appendix D). When *L* is chosen to be 0.8 a, V_m can be minimized to be ~0.004 λ^3, which shows about 2.2 fold reduction from that of the cavity without the nano-slot (*L* = 0). We note that, as the nano-slot width decreases further, the reduction factor for V_m can be brought up to ~7 times [22] (see Appendix E). Interestingly, the condition minimizing V_m maximizes Q_{tot} so that Q_{tot} / V_m can be maximized at the same time. Furthermore, $\eta(\theta = 0)$ in the range of 0.15 ~0.18 is already larger than that from the conventional dipole-antenna radiation, $3/8\pi \cong 0.119$ (see Appendix F), indicating that the efficient inhibition of radiation in the directions parallel to the PhC slab indeed improves the free-space coupling. Inserting all the above values, Q_{tot}, V_m, and η, into Eq. (6), we get considerably large Φ_I of ~783, which is already comparable to those obtained from the metallic SERS active substrates [25,26].

To validate our analytical expression of Eq. (6), we compare our CMT predictions (Fig. 2(c)) to the rigorous FDTD simulation results that incorporate realistic incoming planewaves and subsequent time-evolution of the stored field energy (see Appendix G). As shown in Fig. 2(c), both results agree well with each other indicating that our CMT formalism is valid even for a resonance with *Q* < 100. It should be noted that, however, it may not be applicable to the conventional metallic antennas, because they usually support too low *Q* (typically, <10) [1–4,25,26] to justify the weak-coupling assumption of CMT [18].

3.2 Effects of a bottom reflector

We now consider the effect of a bottom reflector on far-field radiation patterns. In the absence of the bottom reflector, radiation losses occur symmetrically with respect to the PhC slab as shown in Fig. 3(c). If the downward-emitting components could be suppressed, one would double $\eta(\theta = 0)$ as well as the final intensity enhancement, Φ_I (see Eq. (4)). In fact, the gap distance, *d*, is a key parameter to control such enhancement through interferences between the originally upward- and downward-emitting waves, both of which can be met at $\theta = 0$ by the reflector (see Fig. 4a) [16]. As a result, both far-field radiation (or $\eta(\theta = 0)$) and Q_{tot} can be modified. For example, as shown in Fig. 3(d), if *d* equals to the effective 1.0 λ distance ($d = \lambda / n_{bg} = \lambda / 1.33$), fairly-good unidirectional beaming can be obtained [16]. In this regard, our design is reminiscent of the Yagi-Uda antenna [5] in the radio-frequency domain. What is interesting here is that one could achieve very high $\eta(\theta = 0)$ ~0.67 at $d = 0.95\lambda / n_{bg}$ (see Fig. 4(b)), which is about 4 fold enhancement in comparison with that of the PhC cavity without a bottom reflector. Strong modulations in Q_{tot}, V_m, and η as a function of *d* with a periodicity of $\sim 0.5 \times (\lambda / n_{bg})$ are clearly visible, indicating that the far-field interference is associated with the gap size [16].

#135050 - $15.00 USD Received 13 Sep 2010; revised 16 Oct 2010; accepted 21 Oct 2010; published 3 Nov 2010

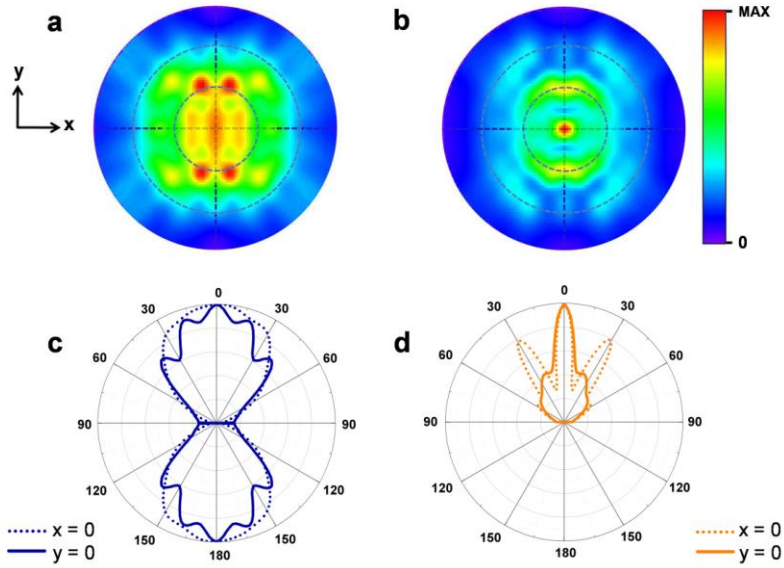

Fig. 3. Far-field radiation patterns. Far-field patterns are calculated by using the finite-difference time-domain method (FDTD) and the near- to far-field transformation formulae presented in ref. 11. The two far-field patterns (*x*,*y*) in the upper row are for the upper hemispherical surface ($0^\circ \le \theta \le 90^\circ$), where the mapping between (*x*,*y*) and (θ , ϕ) is given by $x = \theta\cos\phi$ and $x = \theta\sin\phi$. In the two polar plots in the lower row, the dotted line (solid line) shows the radiation pattern in the *x* = 0 (*y* = 0) plane. (a, c) The photonic-crystal cavity without the bottom reflector, where the length of the nano-slot is 0.8 a. (b, d) The same photonic-cavity cavity as before but with the bottom reflector, where the gap size is $d = \lambda / n_{bg}$.

Similar comparison between our CMT results and rigorous FDTD results has been performed for the PhC antenna with the bottom reflector. For $d < 0.9\lambda / n_{bg}$, the both results seem to agree well with each other. However, as *d* increases further, the CMT prediction begins to fall below the exact FDTD result. The CMT model predicts that the maximum of Φ_I will occur at $d = 0.9\lambda / n_{bg}$ with Φ_I ~3,437. Clearly, the PhC optical antenna outperforms or at least shows similar performances compared with metallic nano-structures [1–6,8,9,25,26]. However, the exact FDTD simulation predicts higher enhancement of ~4,500 at a slightly different gap size of $d = 1.0\lambda / n_{bg}$. Such discrepancy between the two predictions might be due to the fact that the gap region may act as a Fabry-Perot like cavity enclosed by the top PhC slab mirror [16]. This broad resonance may interfere with the narrow resonance of the PhC cavity to produce a Fano-like spectral feature [17]. The result shown in Fig. 4(c) suggests that the more rigorous CMT model incorporating all those interactions should be developed for $d > \sim \lambda / n_{bg}$.

#135050 - $15.00 USD Received 13 Sep 2010; revised 16 Oct 2010; accepted 21 Oct 2010; published 3 Nov 2010

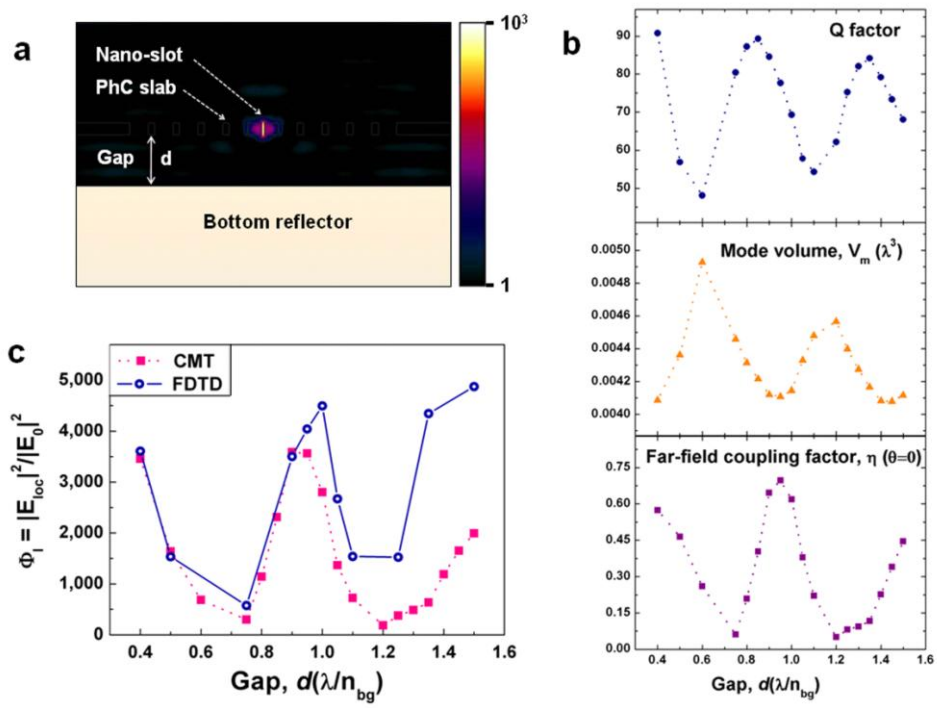

Fig. 4. Effects of the bottom reflector on local-field enhancement. The length of the nano-slot is fixed to be 0.8 a, at which Φ_I has been optimized in the absence of the bottom reflector. (a) Electric-field intensity distribution in the *x-z* plane. The downward-propagating waves can be redirected to the top by the reflector and they can interfere with the originally upward-propagating waves. The interference condition can be determined by the gap size, *d*. (b) Quality factor, Q_{tot}, mode volume, V_m, and the far-field coupling factor, $\eta(\theta = 0)$, calculated as a function of *d*. (c) The electric-field intensity enhancement factors, Φ_I, obtained from the coupled-mode theory (CMT) are compared with those obtained from the rigorous finite-difference time-domain (FDTD) simulation. Φ_I of ~3,437 (~4,500) is obtained from CMT (FDTD) at $d = 0.9\lambda / n_{bg}$ ($d = 1.0\lambda / n_{bg}$).

4. Concluding remarks

The proposed design still leaves room for further improvement. For example, by narrowing the width of the nano-slot, additional factor of 2~3 times Φ_I is achievable. By employing high-*Q* (Q_{tot} > 10,000) modified dipole modes, $\Phi_I > 10^5$ is expected from our CMT model (see Appendix H). For enhancing nonlinear signal generation based on such high-*Q* antennas, one may utilize the multitude of resonances; one for the pumping wavelength and others for the nonlinear-converted wavelengths [27]. Note that such dramatic results do not rely on technologically challenging geometries, such as extremely sharp tips and/or small gaps, which are common features in many metallic antenna designs [1–3,6,19]. Furthermore, one may develop a miniaturized antenna for free-space communication. The similar design can also be applied to high-efficiency photovoltaic devices for driving nano-electronics [28]. The proposed scheme is fully compatible with the matured silicon nanofabrication technique and could be used in a wide range of applications where strong light-and-matter interactions are essential.

#135050 - $15.00 USD Received 13 Sep 2010; revised 16 Oct 2010; accepted 21 Oct 2010; published 3 Nov 2010

Appendix A - Calculation of $|\kappa_0|^2 A$.

According to the known result from Fraunhofer diffraction theory, the finite extent (area A) of an incoming planewave inevitably involves the angular spread, $\Delta\Omega$, such that

$$\Delta\Omega = \frac{(\lambda / n_{bg})^2}{A} \tag{A-1}$$

where λ is the wavelength in vacuum. From the well-known result of CMT [17], we obtain the relation between the coupling constant κ_0 and the partial decay rate $1/\tau_0$ such that $|\kappa_0|^2 = (2/\tau_0)\cos^2\chi$, where χ is the angle between the incident wave's polarization and the outgoing radiation's polarization. The ratio between the power radiated into the solid angle, $\Delta\Omega$, and the total radiated power is given by

$$\frac{\Delta P(\theta \approx 0)}{P_{tot}} = \frac{1/\tau_0}{1/\tau_{tot}}. \tag{A-2}$$

Combining all the above information,

$$|\kappa_0|^2 A = \frac{2}{\tau_0}\left(\frac{\lambda}{n_{bg}}\right)^2 \frac{1}{\Delta\Omega}\cos^2\chi = \frac{2}{\tau_{tot}}\left(\frac{\lambda}{n_{bg}}\right)^2 \frac{\Delta P(\theta \approx 0)}{\Delta\Omega}\frac{1}{P_{tot}}\cos^2\chi \tag{A-3}$$

In the limit of infinitely large area, as both ΔP and $\Delta\Omega$ become infinitesimally small, the above formula equals to Eq. (5).

Appendix B - Definition of mode volume V_m.

The cQED mode volume is defined as the ratio of the total electromagnetic energy stored in the cavity and the peak electromagnetic energy density, such that

$$V_m = \frac{\iiint \frac{1}{2}\varepsilon_0\varepsilon(\vec{r})\left|\vec{E}(\vec{r},t)\right|^2 + \frac{1}{2}\mu_0\left|\vec{H}(\vec{r},t)\right|^2 d^3\vec{r}}{\max\left\{\frac{1}{2}\varepsilon_0\varepsilon(\vec{r})\left|\vec{E}(\vec{r},t)\right|^2 + \frac{1}{2}\mu_0\left|\vec{H}(\vec{r},t)\right|^2\right\}}, \tag{B-1}$$

where we have assumed that the cavity is consisting of non-magnetic materials ($\mu(\vec{r}) = 1$). Taking time averages on both the denominator and the numerator and using the fact, for harmonically oscillating fields, $\left\langle (1/2)\varepsilon_0\varepsilon\left|\vec{E}\right|^2\right\rangle_T = \left\langle (1/2)\mu_0\left|\vec{H}\right|^2\right\rangle_T$, one can rewrite the above expression as

$$V_m = \frac{\left\langle |\alpha|^2\right\rangle_T}{\left\langle \max\left\{\varepsilon_0\varepsilon(\vec{r})\left|\vec{E}(\vec{r},t)\right|^2\right\}\right\rangle_T} = \frac{\left\langle |\alpha|^2\right\rangle_T}{\frac{1}{2}\varepsilon_0 n_c^2\left|\vec{E}_{loc}\right|^2} \tag{B-2}$$

where n_c^2 and $\vec{E}_{loc}$ are the refractive index and the electric-field at the location where the term braced is maximized.

#135050 - $15.00 USD Received 13 Sep 2010; revised 16 Oct 2010; accepted 21 Oct 2010; published 3 Nov 2010

Appendix C - Design of the dipole-mode cavity with $Q < 100$

A single-defect PhC cavity is formed in a 2-D triangular-lattice PhC slab. The slab thickness, T, and the refractive index of the slab, n_{slab}, are chosen to be 0.6 a and 3.5 (that of Si at near-infrared wavelengths), respectively, where 'a' denotes the lattice constant of the PhC. For potential real-time bio-sensing applications, the refractive index of a background material is assumed as water, so $n_{bg} = 1.33$. For a triangular air-hole type PhC slab, the radius of air-holes is usually chosen to be $R \sim 0.35$ a, which allows mechanical robustness as well as wide-enough PBG in the in-plane directions. Throughout the paper, we fix R to be 0.36 a, which gives the in-plane PBG from $\omega_n = 0.27 \sim 0.35$, where ω_n is the normalized frequency, a/λ.

However, without introducing any structural modification, the cavity supports doubly-degenerate dipole-modes (the two dipole-modes are at the exactly same frequency) due to the perfect six-fold symmetry. In order to break the inherent degeneracy and to lower the Q a bit more, we have changed positions of the four-holes as a function of their radii (R_m) such that (see Fig. 5(a))

Modified hole1: $\left(\frac{1}{2}, \frac{\sqrt{3}}{2}\right)a \rightarrow \left(\frac{1+R-R_m}{2}, 0.9\frac{\sqrt{3}}{2}\right)a$

Modified hole2: $\left(\frac{1}{2}, -\frac{\sqrt{3}}{2}\right)a \rightarrow \left(\frac{1+R-R_m}{2}, -0.9\frac{\sqrt{3}}{2}\right)a$

Modified hole3: $\left(-\frac{1}{2}, \frac{\sqrt{3}}{2}\right)a \rightarrow \left(-\frac{1+R-R_m}{2}, 0.9\frac{\sqrt{3}}{2}\right)a$

Modified hole4: $\left(-\frac{1}{2}, -\frac{\sqrt{3}}{2}\right)a \rightarrow \left(-\frac{1+R-R_m}{2}, -0.9\frac{\sqrt{3}}{2}\right)a$

We have investigated how Q and ω_n are evolved as we vary R_m (Fig. 5(b)). Maximizing the strength of in-plane confinement is desirable for higher $\eta(\theta = 0)$. Therefore, we choose R_m to be 0.36 a, which results in Q of ~45. For the deformed dipole mode (R_m = 0.36 a), electric-field intensity distribution ($|\vec{E}|^2$) as well as its electric-field lines are shown in Fig. 5(c). We can see that it has the highest $|\vec{E}|^2$ around the centre of the cavity, where electric-fields are mostly parallel along the x direction. This is the main reason why the dipole-mode has strong vertical radiation with the well-defined linear polarization (x-pol) (see Fig. 5(d)). This fact also provides us an additional hint for further optimization of the mode volume, which will be explained in Appendix E. It is a known fact that the other degenerate-split dipole pair is orthogonally polarized (y-pol) to this dipole-mode [11].

#135050 - $15.00 USD Received 13 Sep 2010; revised 16 Oct 2010; accepted 21 Oct 2010; published 3 Nov 2010

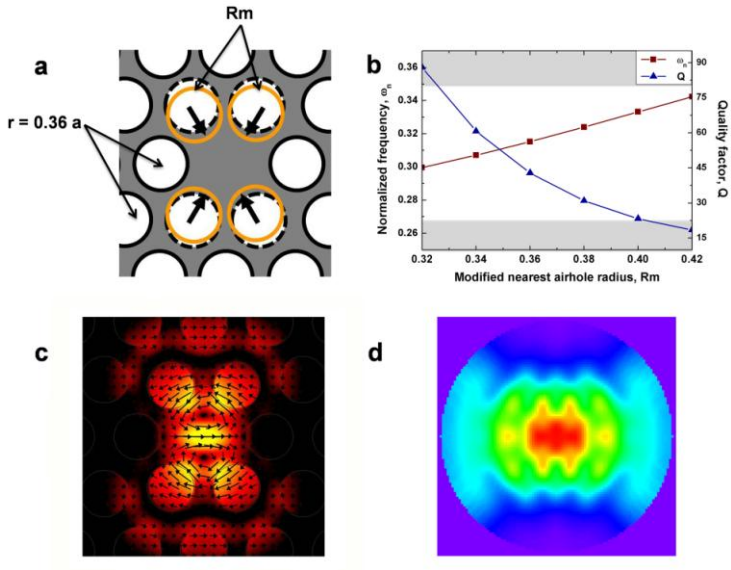

Fig. 5. (a) Structure of the low-*Q* dipole mode cavity. (b) Normalized frequency and Quality factor as a function of the modified hole radius, R_m. (c) Vector plot of the electric-fields. (d) Far-field radiation pattern from the mode shown in Fig. 5(c).

Appendix D - Tuning of the PhC cavity by varying the length of a nano-slot

Figure 6 shows evolution of the normalized frequency (ω_n) and the resonant wavelength (in case of a = 350 nm) as a function of the slot length (*L*). In this paper, the width of the nano-slot is fixed to 0.05 a, which corresponds to 17.5 nm. When *L* is varied between 0.6 a and 1.0 a, the resonant wavelength is quite stable at ~ 1,095 nm. Slight tuning the lattice constant by about 2% will bring down the resonant wavelength to 1,064 nm, which is suited for Nd:YAG laser pumping.

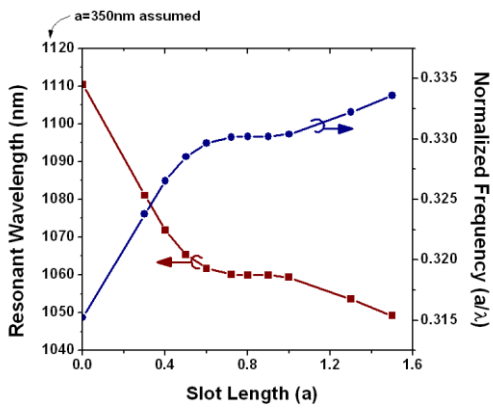

Fig. 6. Resonant wavelength (nm) and normalized frequency (a/λ) as a function of the slot length (a), where a = 350 nm was assumed.

Appendix E - Introduction of a nano-slot into a PhC cavity

As shown in Fig. 2(a), we introduce the nano-slot in the region where electric-fields are aligned along the *x* direction. If the width of it is sufficiently small not to perturb the original field distribution too much, then we can safely assume that the electric-fields are still aligned in the same direction. However, the amplitude of the electric-field within the slot can be changed noticeably due to the boundary condition for the normal components of the electric-

#135050 - $15.00 USD Received 13 Sep 2010; revised 16 Oct 2010; accepted 21 Oct 2010; published 3 Nov 2010

fields. The similar idea was proposed by J. T. Robinson, *et al.* and applied to 1-D nanobeam cavities [22]. Here, we briefly discuss how the nano-slot can reduce the mode volume.

First let us recall the boundary condition for normal components of the electric-field on either side of the boundary surface (at $x = \pm\Delta/2$),

$$n_{slab}^2 E_x(x = \Delta/2) \cong n_{bg}^2 E_x^{'}(x = \Delta/2). \tag{E-1}$$

Here E_x and $E_x^{'}$ are the electric-fields before and after introducing the nano-slot at the centre of the cavity, respectively. We also assume that the width of the slot is so small ($\Delta \to 0$) that it could not change the total electromagnetic energy contained in the cavity. From the definition of the cQED mode volume, before introducing the nano-slot, we have

$$V_m = \frac{\left\langle |\alpha|^2 \right\rangle_T}{\frac{1}{2}\varepsilon_0 n_{slab}^2 \left|E_x(x=0)\right|^2}. \tag{E-2}$$

After introducing the nano-slot, however,

$$V_m^{'} = \frac{\left\langle |\alpha|^2 \right\rangle_T}{\frac{1}{2}\varepsilon_0 n_{bg}^2 \left|E_x^{'}(x=0)\right|^2} \cong \left(\frac{n_{bg}}{n_{slab}}\right)^2 V_m. \tag{E-3}$$

Therefore, for an ideal nano-slot ($\Delta \approx 0$), the maximum reduction in the mode volume could be up to $(n_{slab}/n_{bg})^2 = (3.5/1.33)^2 \approx 6.9$.

Appendix F - Examples of the far-field coupling factor, η

For isotropic radiation pattern over the entire 4π steradian (ideal spherical source)

Because $dP/d\Omega$ is a constant, $P_{tot} = \int \frac{dP}{d\Omega} d\Omega = \frac{dP}{d\Omega}\int d\Omega = 4\pi \frac{dP}{d\Omega}$. Therefore, we get $\eta(\theta,\phi) = \eta(\theta = 0) = 1/4\pi \cong 0.0796$

For classical dipole antenna radiation

$dP/d\Omega$ is given by $dP/d\Omega = (3P_{tot}/8\pi)\sin^2(\pi/2 - \theta)$, where the direction of the dipole oscillation is assumed to be in the *x*-*y* plane. Therefore, $\eta(\theta = 0) = 3/8\pi \cong 0.119$.

Appendix G - Calculation of Φ_I using FDTD

In order to estimate the electric-field intensity enhancement (Φ_I) through Eq. (6), the three important parameters, Q, V_m, and $\eta(\theta = 0)$, should be obtained by using FDTD.

Cavity Q

E_x-field component at the center of the cavity has been detected as a function of time. Then the harmonic inversion algorithm (harminv) [29] is used to obtain *Q*.

Mode volume V_m

For sufficiently high-*Q* modes, both of the following definitions will produce the almost same values.

#135050 - $15.00 USD Received 13 Sep 2010; revised 16 Oct 2010; accepted 21 Oct 2010; published 3 Nov 2010

$$V_m^{(1)} = \frac{\iiint \varepsilon_0 \varepsilon(\vec{r}) \left|\vec{E}(\vec{r}, t_m)\right|^2 d^3\vec{r}}{\max\left\{\varepsilon_0 \varepsilon(\vec{r}) \left|\vec{E}(\vec{r}, t_m)\right|^2\right\}}, \tag{G-1}$$

$$V_m^{(2)} = \frac{\left\langle \iiint \varepsilon_0 \varepsilon(\vec{r}) \left|\vec{E}(\vec{r}, t)\right|^2 d^3\vec{r} \right\rangle_T}{\left\langle \max\left\{\varepsilon_0 \varepsilon(\vec{r}) \left|\vec{E}(\vec{r}, t)\right|^2\right\}\right\rangle_T} \tag{G-2}$$

Here, in the first definition, t_m is the time when harmonically varying electric-fields are maximized. In the second definition, time averages are performed over one optical period. However, for low-Q modes, differences between $V_m^{(1)}$ and $V_m^{(2)}$ become more pronounced because of the fast decay of the fields within one optical cycle. We have used the second expression, $V_m^{(2)}$, for our definition of the mode volume (see also Appendix B).

Far-field coupling factor, $\eta(\theta = 0)$

As depicted in Fig. 7(a), we set up a small area (S_0 = $(a/40)\times(a/40)$) which locates sufficiently far away from the cavity (L_z > 3λ). Then, the power radiated through the whole surface (S_{tot}) and the power radiated through the small area (S_0) are obtained during FDTD time stepping. Using the definition of $\eta(\theta = 0)$ (see Eq. (4)),

$$\eta(\theta = 0) = \frac{\left.\frac{dP}{d\Omega}\right|_{\theta=0}}{P_{tot}} = \left(\frac{\text{Power radiated through } S_0}{S_0 / L_z^2}\right) \times \frac{1}{\text{Power radiated through } S_{tot}} \tag{G-3}$$

Rigorous FDTD simulation for Φ_I

As depicted in Fig. 7(b), a continuous-wave (CW) planewave source ($\left|\vec{E}_0\right|^2$) which is polarized along the x direction is generated and propagated onto the PhC cavity. We detect $\left|\vec{E}_{loc}(t)\right|^2$ as a function of time at the centre of the slot until it reaches a certain steady-state value. Then, we compute the ratio between $\left\langle \left|\vec{E}_{loc}(t \to \infty)\right|^2 \right\rangle_T$ and $\left\langle \left|\vec{E}_0\right|^2 \right\rangle_T$ to get the enhancement factor, Φ_I .

#135050 - $15.00 USD Received 13 Sep 2010; revised 16 Oct 2010; accepted 21 Oct 2010; published 3 Nov 2010

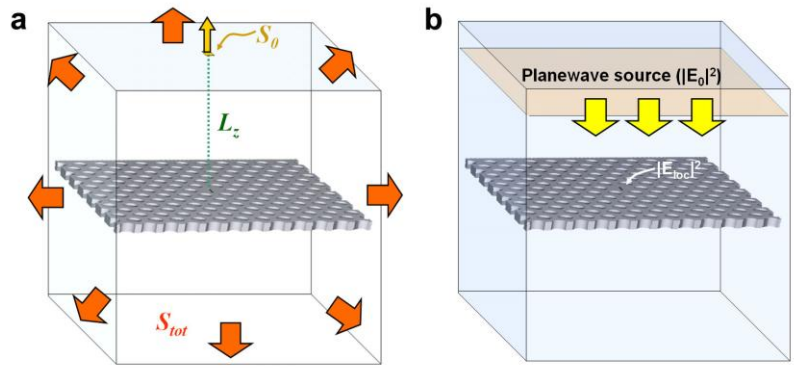

Fig. 7. (a) FDTD simulations used to obtain the far-field coupling factor, η. (b) The rigorous FDTD simulation used to directly obtain Φ_t.

Appendix H - Extremely large local-field enhancement > 10^5 from the modified dipole mode

We have designed a high-*Q* dipole mode by modifying the six nearest neighbor holes as depicted in Fig. 8(a). The slab thickness, *T*, and the refractive index of the slab, n_{slab}, are the same as before. The entire device is assumed to be completely immersed in water (n_{bg} = 1.33). The radius of background air-holes is chosen to be r = 0.35 a and the six nearest holes are slightly pushed away from the cavity center after reducing their radii to r_m = 0.28 a. To estimate resultant local electric-field intensity enhancement, we have used Eq. (6). Three important parameters, Q, V_m, and $\eta(\theta = 0)$, along with the resultant field enhancement values are presented in Table 1 for several representative cases with and without a bottom mirror.

Table 1. Electric-field intensity enhancement from the high-*Q* dipole mode.

	Without a mirror	Effective gap 0.95 λ	Effective gap 1.00 λ	Effective gap 1.05 λ
Q_{tot}	5812	5464	5261	5256
V_m (λ^3)	0.00315	0.00316	0.00315	0.00315
$\eta(\theta = 0)$	0.1956	0.2267	0.2989	0.2850
$\lvert \boldsymbol{E}_{loc}\rvert^2/\lvert \boldsymbol{E}_0\rvert^2$	**97,682**	**106,246**	**134,948**	**128,632**

It is noteworthy that $\eta(\theta = 0)$ has been compromised with the high-*Q*, to a relatively low value of ~0.3. However, owing to their high *Q/V* values, one can achieve extremely high electric-field intensity enhancements over 100,000. Highly localized electric-field intensity distributions within the nano-slot are shown in Fig. 8(b) and Fig. 8(c).

#135050 - $15.00 USD Received 13 Sep 2010; revised 16 Oct 2010; accepted 21 Oct 2010; published 3 Nov 2010

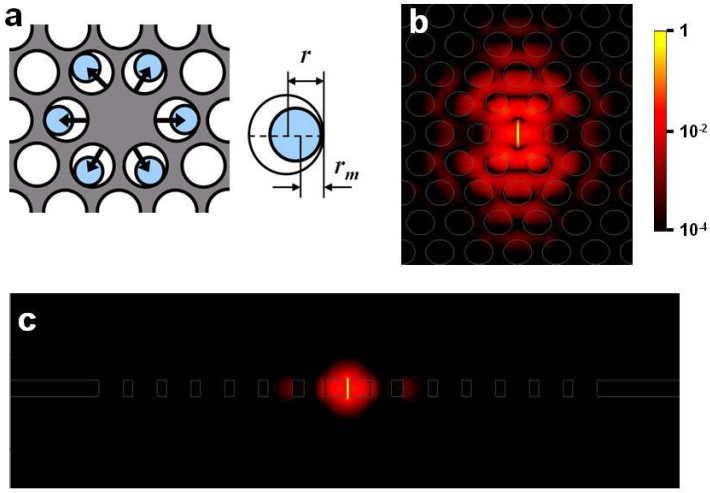

Fig. 8. (a) Structure of the high-*Q* PhC dipole mode cavity. (b,c) Electric-field intensity ($|\mathbf{E}|^2$) distributions (b) in the *x*-*y* plane and (c) in the *x*-*z* plane.

Acknowledgments

This work was supported by the Korea Research Foundation Grant funded by the Korean Government (KRF-2008-357-C00042), the Defense Advanced Research Projects Agency through W911NF-07-1-0277, the Boeing through CT-BA-GTA-1, and the National Institutes of Health through 4R00EB007151-03.